

Supporting Information for:
Transformation of TiO₂ (nano)particles during sewage
sludge incineration

Jonas Wielinski^{a,b}, Andreas Voegelin^a, Bernard Grobety^c, Christoph R. Müller^d,
Eberhard Morgenroth^{a,b} and Ralf Kaegi^{a*}

Accepted on December 19, 2020

^aEawag, Swiss Federal Institute of Aquatic Science and Technology, 8600 Dübendorf, Switzerland

^bETH Zürich, Institute of Environmental Engineering, 8093 Zürich, Switzerland

^cUniversity of Fribourg, Department of Geosciences, 1700 Fribourg, Switzerland

^dETH Zürich, Institute of Energy Technology, 8092 Zürich, Switzerland

Corresponding author:

*Ralf Kaegi, ralf.kaegi@eawag.ch, Tel.: +41 58 765 5273, Eawag, Überlandstrasse 133, 8600 Dübendorf, Switzerland.

This Supporting Information document contains:

- 20 pages,
- 14 figures, and
- 7 tables.

Contents

S1 Spiking materials: size determination and phase confirmation.	S3
S2 Elemental composition of experimental samples.	S7
S3 EuTiO_3 characterization and origin of the other reference materials	S8
S4 Confirmation of the appropriateness of the FDM calculations	S10
S5 A collection of reference material spectra	S12
S6 Details of mass balance calculations	S13
S7 Principle component analysis and target testing	S13
S8 Detailed analysis of the LCF data.	S14
S9 The Ti speciation in selected soil samples	S15
S10 Supporting synchrotron XRF data on a related sample.	S17
S11 Semi-quantitative Rietveld analysis of sample A-af	S17

List of Figures

S1 Anatase SEM image.	S3
S2 Rutile SEM image.	S4
S3 XRPD patterns of anatase and rutile.	S5
S4 XAS data of anatase and rutile.	S6
S5 XRPD pattern of EuTiO_3	S8
S6 <i>Ab initio</i> calculated rutile XANES spectrum.	S10
S7 <i>Ab initio</i> calculated ilmenite XANES spectrum.	S11
S8 XAS data of reference materials.. . . .	S12
S9 Loadings of principle components.	S13
S10 XANES LCF to spectra of soil samples.. . . .	S16
S11 Bicolor map of Ti and Fe distribution in fly ash.. . . .	S18
S12 Spatial distribution of Ti.	S18
S13 XRPD pattern recorded on fly ash.	S19
S14 Results of Rietveld refinement to XRPD pattern recorded on fly ash.. . . .	S19

List of Tables

S1 Elemental data of experimental samples.	S7
S2 Reference material origins.	S9
S3 Details of the mass balances.	S13
S4 Results of the target transform (TT).. . . .	S13
S5 LCF results of sludge and ash.	S14
S6 LCF results of spiked sludge and ash.. . . .	S14
S7 Information on the origin soil samples.. . . .	S15

S1 Spiking materials: size determination and phase confirmation

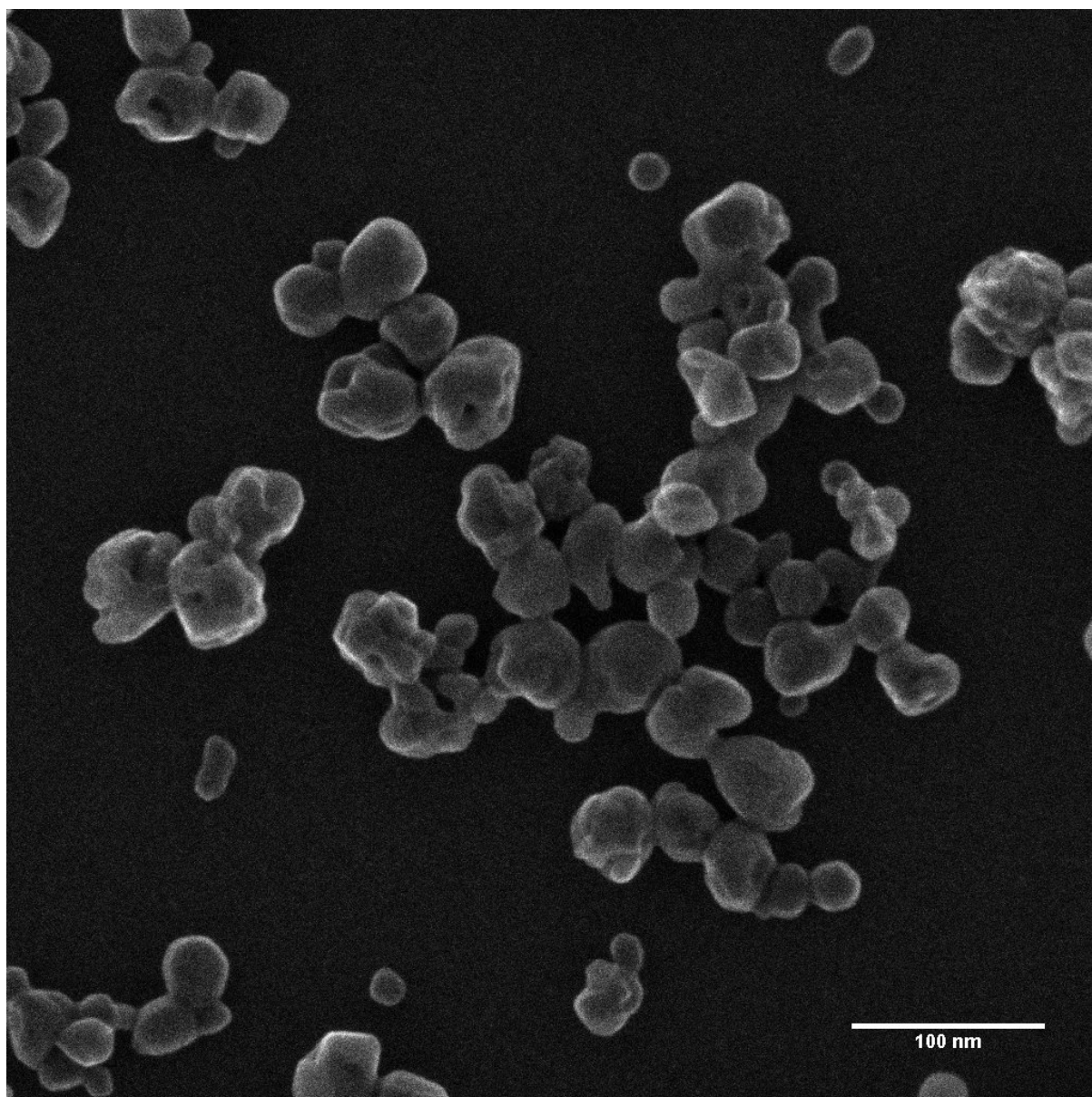


FIGURE S1. Secondary electron image of the anatase nano particles spiked to the sludge.

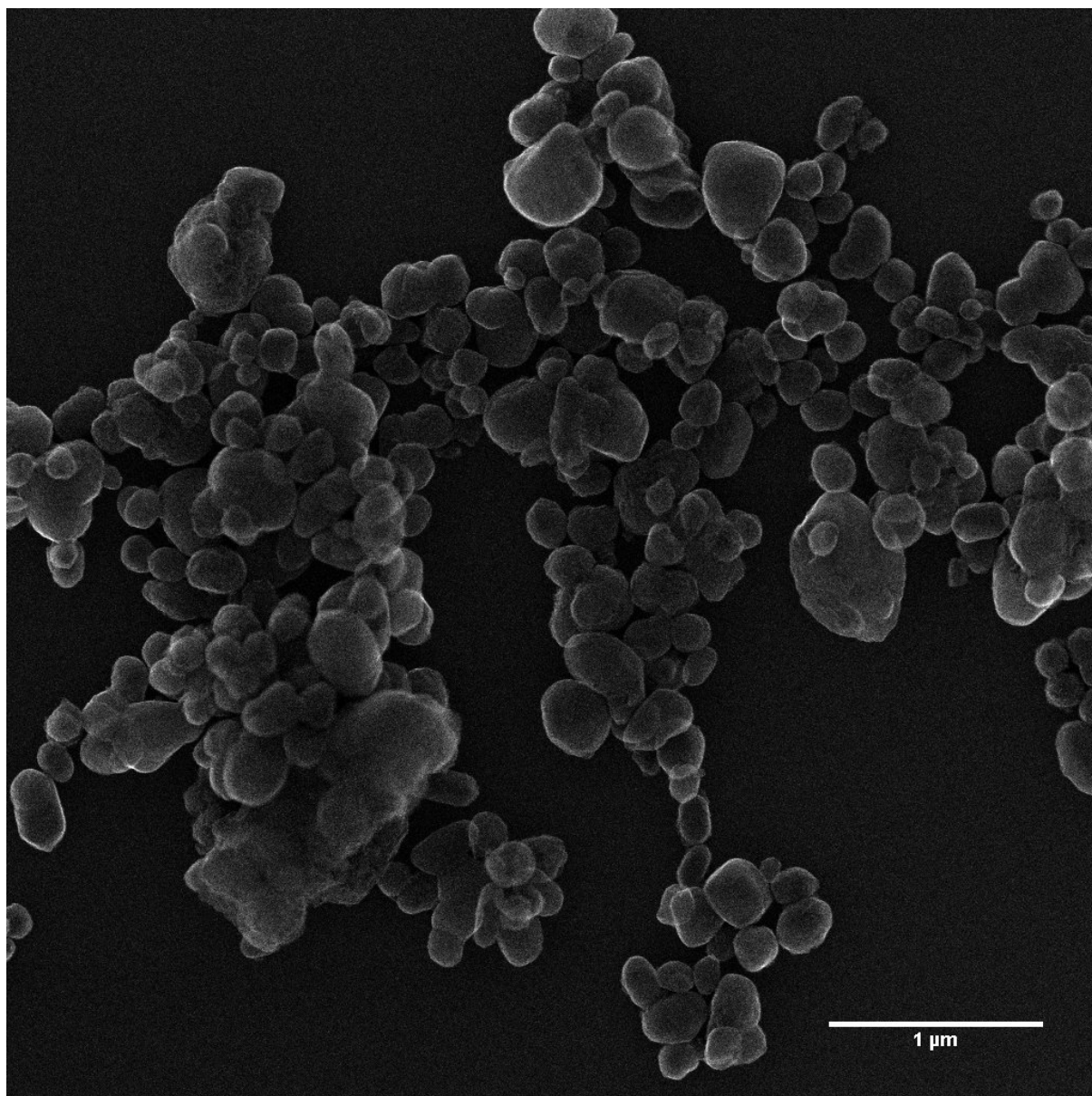


FIGURE S2. Secondary electron image of the rutile particles spiked to the sludge.

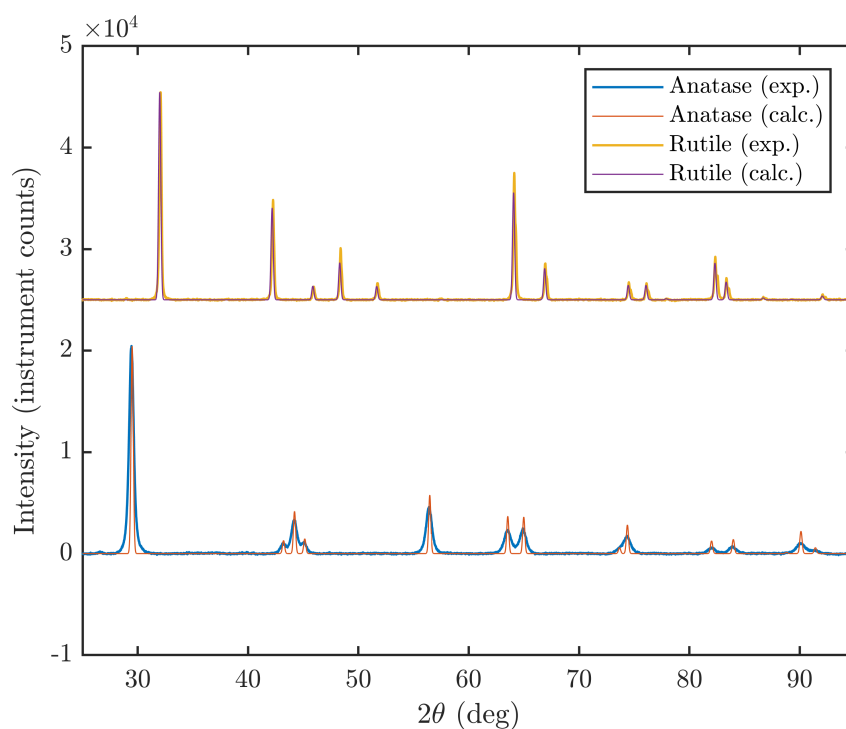


FIGURE S3. Experimental XRPD patterns of anatase (blue) and rutile (yellow). Note the broader peaks in anatase resulting from the smaller crystallite sizes. Data collection parameters are given in section 2.7. Simulated but not refined reflections based on crystallographic data of anatase 1 and rutile 2 obtained through the Inorganic Crystal Structure Database (ICSD) are drawn in red and purple, respectively.

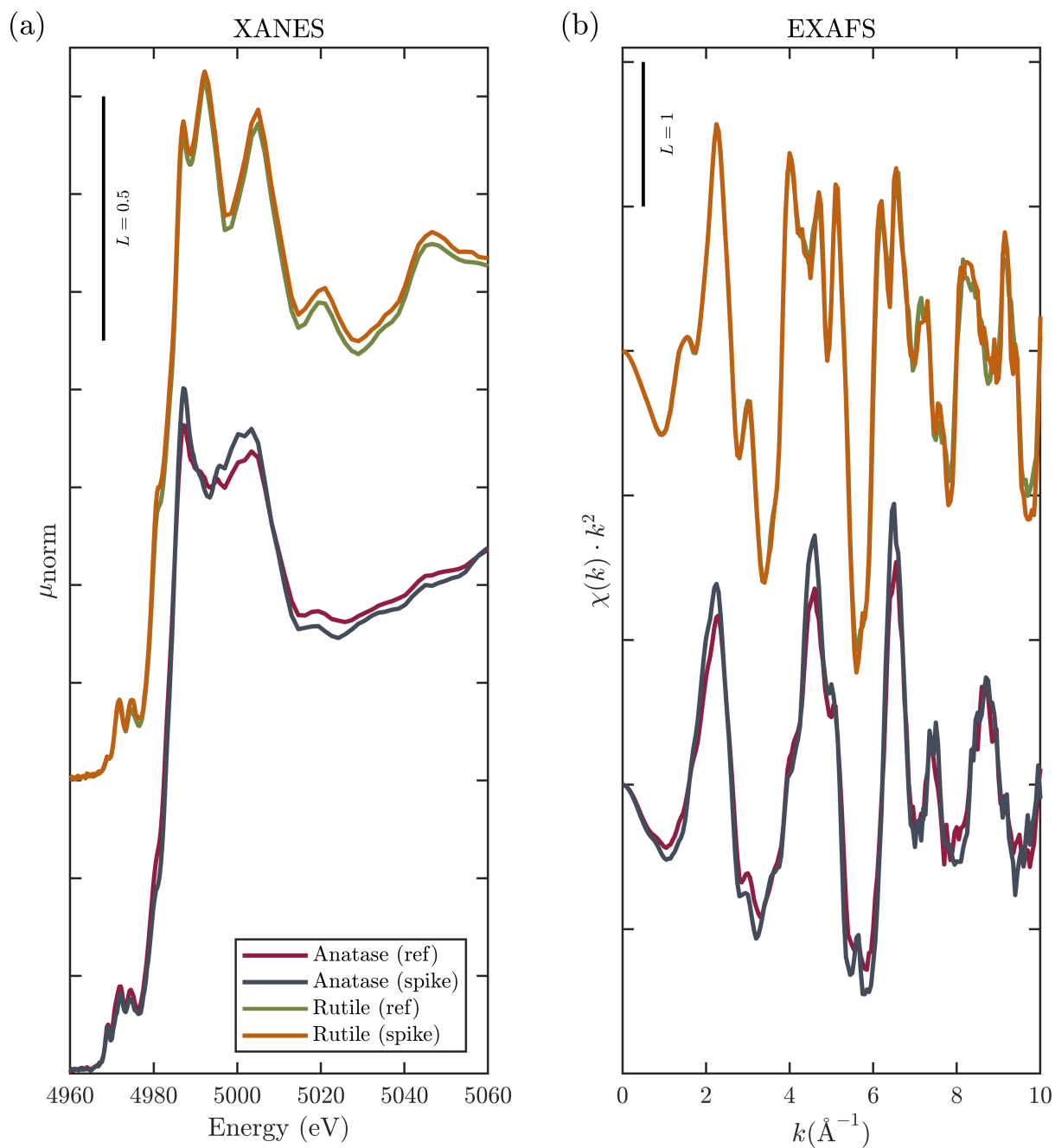


FIGURE S4. (a) XANES and (b) EXAFS data of the spiked materials and high purity reference nano materials of the same crystal structure.

S2 Elemental composition of experimental samples

TABLE S1. Elemental concentrations (Ti, Fe, Ca, Sr, Ba and Pb) of the samples as determined by X-ray fluorescence (XRF). An explanation of the sample abbreviation is given to the right.

Sample name	Ti (mg/kg)	Fe (%)	Ca (%)	Sr (mg/kg)	Ba (mg/kg)	Pb (mg/kg)	Explanation of the sample
A-af	4100	14.35*	10.26	443.9	907	66.9	Ash collected from full-scale incineration plant Werdhölzli.
A-ap-b	6200	25.05	16.75	645.2	2544	108.1	Bottom ash produced in the pilot FBR derived from sludge collected at WWTP Werdhölzli.
A-ap	3300	18.55	11.43	491.4	1321	137.1	Fly ash produced in the pilot FBR derived from sludge collected at WWTP Werdhölzli.
A-s	1800	8.28	5.04	215.2	636.9	40.1	Sludge collected at WWTP Werdhölzli.
An-ap-b	23800	15.96	12.5	482.7	1013	33.6	Bottom ash produced in the pilot FBR derived from sludge spiked with nano anatase.
An-ap	7100	16.19	9.49	346	493	107.8	Fly ash produced in the pilot FBR derived from sludge spiked with nano anatase.
An-s	7300	5.29	4.04	161	380.5	20.8	Sludge (S) spiked with nano anatase.
B-af	4500	17.13	9.19	417.5	761	128.7	Ash collected from full-scale incineration plant ProRhen.
B-ap-b	3900	12.97	9.93	484.5	671	83.6	Bottom ash produced in the pilot FBR derived from sludge collected at WWTP ProRhen.
B-ap	4500	17.64	12.09	600.6	817	237.4	Fly ash produced in the pilot FBR derived from sludge collected at WWTP ProRhen.
B-s	1300	4.53	3.22	163.4	280.9	38.7	Sludge collected at WWTP ProRhen.
C-af	1600	11.18	14.25	284.4	289	71.6	Ash collected from full-scale incineration plant ARA Rhein.
C-ap-b	2100	12.39	10.08	198.2	214.4	6.9	Bottom ash produced in the pilot FBR derived from sludge collected at WWTP ARA Rhein.
C-ap	2400	13.68	10.84	265.9	466.1	206.2	Fly ash produced in the pilot FBR derived from sludge collected at WWTP ARA Rhein.
C-s	1000	5.66	4.67	88.7	135.2	17.8	Sludge collected at WWTP ARA Rhein.
Ru-ap-b	28100	14.85	11.31	446	795.1	58.5	Bottom ash produced in the pilot FBR derived from sludge spiked with rutile pigments.
Ru-ap	12400	13.88	8.19	291.2	574.6	136.1	Fly ash produced in the pilot FBR derived from sludge spiked with rutile pigments.
Ru-s	8700	5.7	3.92	155.6	338.1	20.5	Sludge (S) spiked with rutile pigments.
S	1000	4.9	3.97	163.4	368.1	20.4	Sludge spiked with anatase or rutile.

S3 EuTiO_3 characterization and origin of the other reference materials

The crystal structure of the synthesized reference material EuTiO_3 was confirmed by X-ray powder diffraction (XRPD, section 2.7 main text). Rietveld refinement to identify structural deviations from published data were performed using the X'Pert Highscore Plus software (PANalytical). Scale factor, profile width and cell parameter were refined. All reflections indicated by the published data were found (Figure S5a). The sum of the normalized squared residuals of $R^2 = 0.0253$ was deemed acceptable and the residuals are given in Figure S5b. Three minor reflections at 42.15° , 48.27° and 64.08° , that did not result from the EuTiO_3 powder indicated the presence of minor impurities. However, as the respective intensities were rather low, the phases were thus not considered any further. The space group of EuTiO_3 is $\text{Pm}\bar{3}\text{m}$, cell parameter is $a = b = c = 3.9082 \text{ \AA}$ and $\alpha = \beta = \gamma = 90^\circ$ (Köhler et al., 2012). The refined cell parameter was 3.90167 \AA , which is sufficiently close to the published data.

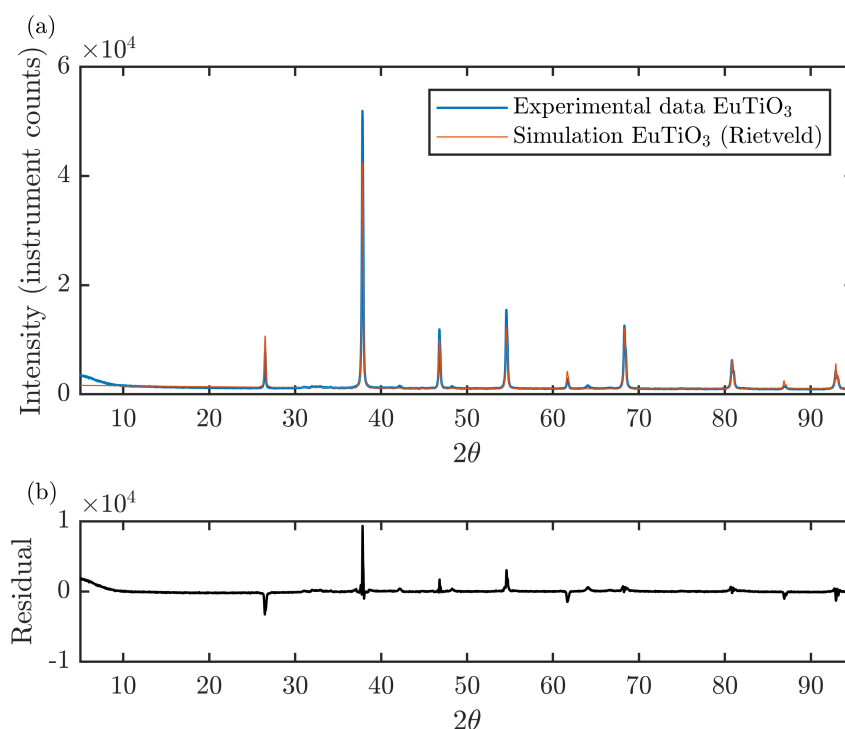


FIGURE S5. XRPD diffractogram of EuTiO_3 . Experimental data is shown as blue lines, Rietveld refined simulation is shown in red.

TABLE S2. Information about the origin and purities of the reference materials for XAS analysis.

Name	Origin	Grade as indicated by the manufacturer
Anatase	Sigma-Aldrich	99.7% trace metal basis
Rutile	Sigma-Aldrich	99.5% trace metal basis
Brookite	Sigma-Aldrich	99.99% trace metal basis
CaTiO ₃	MaTecK	99% purity
FeTiO ₃	Merck	99.90%
BaTiO ₃	MaTecK	99.99% purity
SrTiO ₃	Merck	99%
PbTiO ₃	MaTecK	99.9% purity
Ti ₂ O ₃	Merck	99.9% trace metal basis
Ti(IV)sulfate	Fischer Scientific	Ca. 15%, technical grade
Ti(III)sulfate	Fischer Scientific	Ca. 15%, technical grade

S4 Confirmation of the appropriateness of the FDM calculations

Ab initio XANES of rutile and ilmenite were calculated. At least 150 atoms ($r = 7.2 \text{ \AA}$) were considered in the calculations. Self-consistent field (SCF) calculations were performed prior to the finite difference method (FDM) calculations in which dipole and quadrupole transitions were considered.

Rutile. The seven vertical lines indicate features (f1 - f7) of the experimental spectrum that will be compared to the features of the calculated XANES (Figure S6). f1 to f3 represent the pre-edge region, f4 the edge and f5 to f7 the post-edge XANES. The theoretical XANES reproduces all f2 - f7 well, only f1 is shifted to lower energies and had higher intensity compared to the experimental spectrum.

Ilmenite. In the experimental spectrum, we identified six relevant features (f1 - f6, Figure S7). f2 - f6 are well reproduced by the theoretical spectrum, however, f1 is lacking in the calculated spectrum. f1 occurs at 3 eV, whereas the corresponding feature in the theoretical XANES occurs at 4 eV.

In conclusion, the theoretical rutile spectrum presented by Kravtsova et al. (2010) was successfully reproduced and, using the same parameters for SCF and FDM, we were able to produce a theoretical ilmenite spectrum.

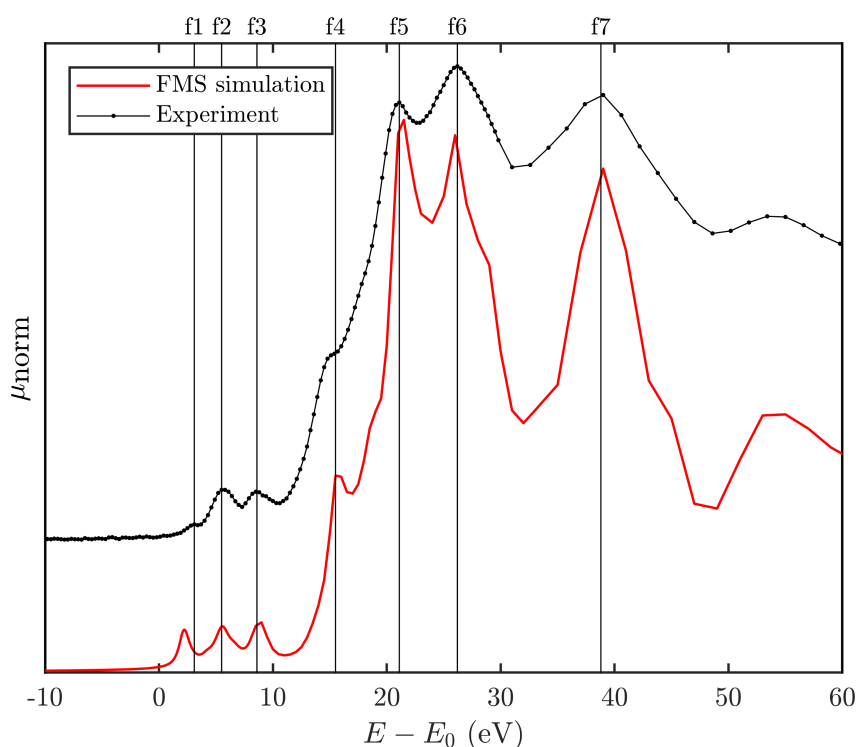


FIGURE S6. Result of the FDM calculation of rutile (red line) compared to the experimental data (black, dots/line). The numbers 1 to 7 above the graph indicate features discussed in the text. The spectra were aligned with respect to f2.

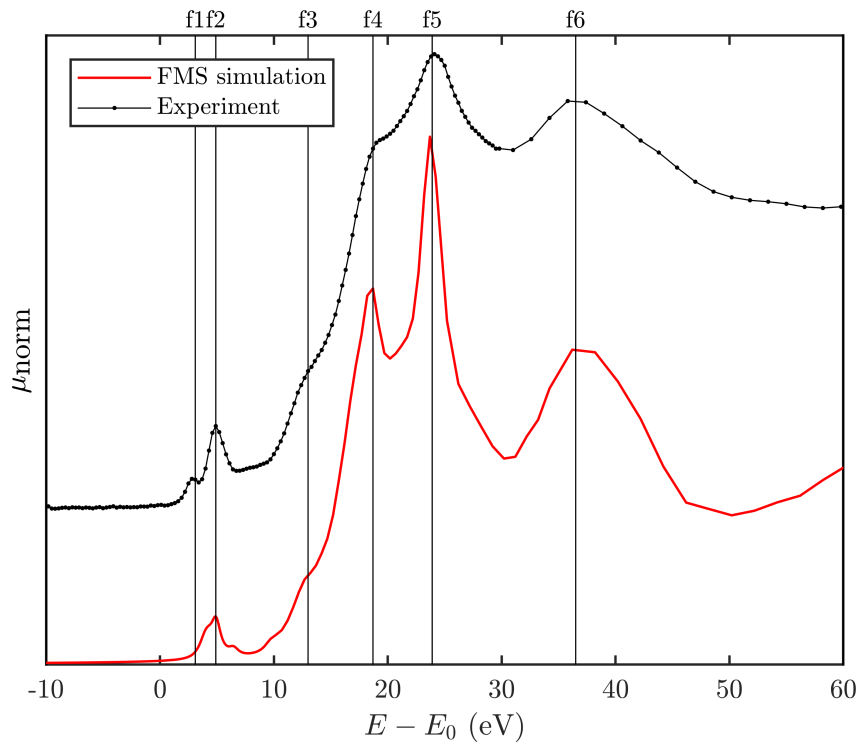


FIGURE S7. Result of the FDM calculation of ilmenite (red line) compared to the experimental data (black, dots/line). The numbers 1 to 6 above the graph indicate features discussed in the text. The spectra were aligned with respect to f2.

S5 A collection of reference material spectra

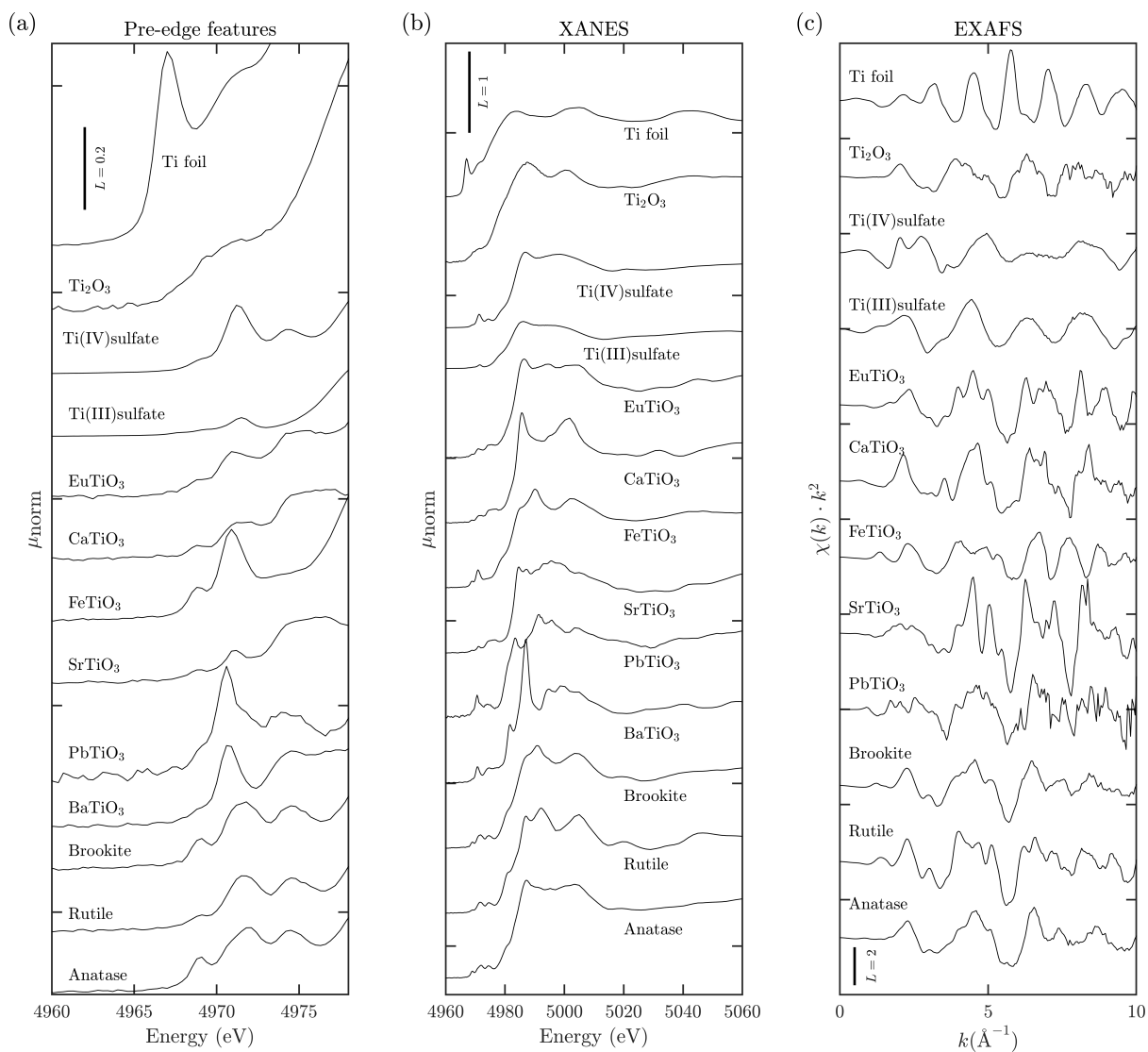


FIGURE S8. (a) Pre-edge features, (b) XANES and (c) EXAFS of all recorded reference material spectra. The EXAFS of BaTiO_3 is not shown due to the strong interference of the Ba L_{III} -edge.

S6 Details of mass balance calculations

TABLE S3. Details of the mass balances. All concentrations (c_x) are Ti concentrations taken from Table S1. The value of $\chi_{TS}\chi_{ash}$ for sample "S" was 33.1%. * value taken from Wielinski et al. (2019).

	m_{sludge} (g)	m_{fly} (g)	m_{bottom} (g)	χ_{TS}	χ_{ash}	$\chi_{TS} \chi_{ash}$	c_{sludge} (%)	c_{fly} (%)	c_{bottom} (%)	Recovered ash content (%)	Recovery of Ti	EF
A	1000.00*	51.00*	275.70*	0.940*	0.319*	30%*	0.18%	0.33%	0.62%	109%*	104%	3.2
B	1000.00*	43.60*	362.60*	0.940*	0.443*	42%*	0.13%	0.45%	0.39%	98%*	131%	3
C	800.00*	14.60*	289.30*	0.940*	0.350*	33%*	0.10%	0.24%	0.21%	115%*	69%	2.1
An	500	38.72	161.13	-	-	35%	0.73%	0.71%	2.30%	115%	95%	2.7
Ru	500	19.99	122.15	-	-	34%	0.87%	1.24%	2.81%	84%	101%	3

S7 Principle component analysis and target testing

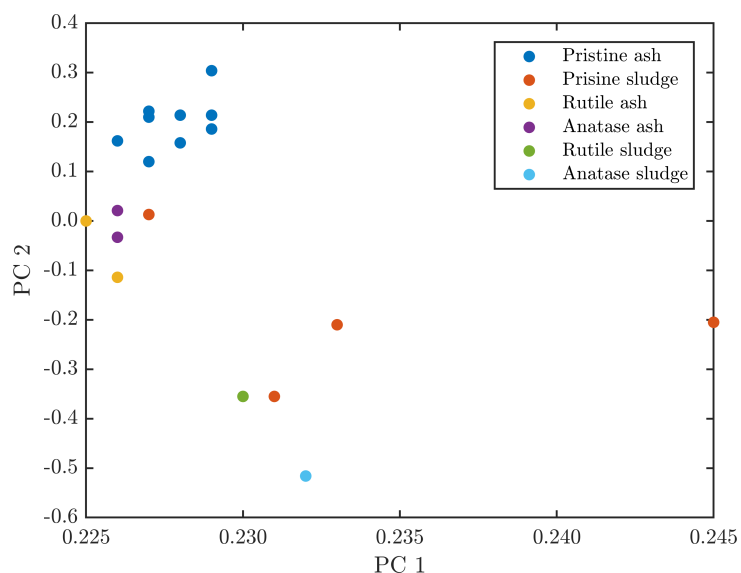


FIGURE S9. Loadings of the principle component (PC) 1 versus PC 2 for all sludge and ash samples.

TABLE S4. Results of the target transform (TT) using the first two PCs.

	χ^2	R-value	SPOIL
Anatase	0.7605	0.0054	5.4934
Brookite	0.4409	0.0031	4.1457
CaTiO3	8.3072	0.0549	18.3068
EuTiO3	1.7021	0.0115	8.1247
FeTiO3	0.6818	0.0051	1.7524
PbTiO3	9.0889	0.0454	7.8913
Rutile	0.685	0.0047	2.4035
SrTiO3	6.2454	0.0381	12.7172
Ti2O3	10.8304	0.0914	5.8092
BaTiO3			
Ti(III) sulfate	10.3735	0.0718	7.9876
Ti(IV) sulfate	1.9053	0.0153	5.4859

S8 Detailed analysis of the LCF data

As received samples. Here, we discuss the results of LCFs to the Ti XANES spectra recorded on as received sludge and the respective ash samples (section 3.2.2 main text). We used all reference material spectra with SPOIL values below 6 for the fits (Table S4), however, neither brookite nor Ti_2O_3 improved the fit quality and these phases were thus not included in the analyses (data not shown). In A-s and B-s, rutile (red) and anatase (yellow) were the most important reference material spectra contributing to the sample spectra (Figure 2 main text). The contribution of the Ti(IV)sulfate spectrum is prominent in A-s (violet, 20%). C-s can be described by comparable shares of anatase, rutile and Ti(IV)sulfate spectra. The contribution of the FeTiO_3 reference spectrum was of minor importance (16%). The fits matched the collected spectra well (Table S5).

In contrast, in the LCFs to the ash spectra, the most important oscillations were not well reproduced by the reference material spectra. A significant mismatch was observed around the pre-edge features (vertical line, f1, Figure 2a main text) and for the most prominent oscillation (f3). The oscillation in f3 was only observable in the spectrum on FeTiO_3 . Between 31 and 40% of FeTiO_3 were fitted to the ash spectra. The pre-edge feature observed in the FeTiO_3 spectrum (f1) was almost identical to those of the ash spectra (detailed discussion in section 3.2.3 main text).

TABLE S5. Results from the LCFs to the sludge and ash samples. The results are displayed graphically in Figure 2 (main text).

	FeTiO_3	Rutile	Anatase	Ti(IV)sulfate	R-factor	χ^2	Red χ^2
A-af	40%	37%	9%	14%	0.002594	0.000772	0.08879
A-ap	31%	33%	25%	4%	0.001574	0.000398	0.04582
A-ap-b	33%	34%	17%	9%	0.002083	0.000524	0.06021
A-s	1%	45%	33%	21%	0.001044	0.000307	0.03528
B-af	38%	32%	14%	11%	0.002281	0.000587	0.06746
B-ap	39%	27%	21%	6%	0.00222	0.000564	0.06483
B-ap-b	38%	26%	19%	10%	0.002222	0.000561	0.0645
B-s	0%	45%	49%	0%	0.000972	0.000256	0.02918
C-af	35%	13%	46%	0%	0.001585	0.000357	0.05824
C-ap	35%	13%	45%	0%	0.002565	0.000658	0.07566
C-ap-b	39%	14%	41%	0%	0.003739	0.000857	0.13965
C-s	16%	23%	25%	32%	0.00056	0.000126	0.02048

Spiked samples. Here, the LCF results (Table S6) are only discussed in the main text.

TABLE S6. Results of the linear combination fits to the samples of the spiking experiment. The results are displayed in Figure 4 (main text).

Sample	Anatase	Rutile	Merged ash	Ti(IV) sulfate	R-factor	χ^2	Red χ^2
S	39%	54%	7%	0%	0.0007597	0.02283	0.0002003
An-s	89%	10%	0%	1%	0.0009875	0.02910	0.0002598
An-ap	20%	20%	40%	21%	0.0002628	0.00750	0.0000670
An-ap-b	17%	15%	44%	24%	0.0003938	0.01148	0.0001007
Ru-s	4%	93%	3%	0%	0.0024219	0.07438	0.0006524
Ru-ap	12%	60%	24%	4%	0.0004918	0.01423	0.0001270
Ru-ap	3%	41%	37%	19%	0.0005411	0.01575	0.0001382

S9 The Ti speciation in selected soil samples

The goal of this analysis was to demonstrate that the available reference material spectra are sufficient to describe the Ti phases in different types of soils and thus to evaluate whether the spectra of Ti phases formed during incineration are different from those found in the natural environment. In this case, XANES (and EXAFS) spectra could be used as finger prints for the presence of incineration residues. To obtain the Ti speciation in a range of soils, we selected 6 soil samples (So1 - So6) from the Swiss Soil Monitoring Network (NABO) for XAS measurements (Table S7, Figure S10).

In soils, Ti is known to occur in rutile, anatase, ilmenite, perovskite and pseudo-rutile ($\text{Fe}_2\text{O}_3 \cdot n\text{TiO}_2 \cdot m\text{H}_2\text{O}$; $3 < n < 5$ and $1 < m < 2$) a weathering product from ilmenite (Scheinost, 2005), but a pseudo-rutile reference spectrum was not available. Thus, we used the frequently found minerals and Ti(IV)sulfate as representative of a distorted octahedrally coordinated Ti phase for LCFs. The Ti spectra of the soils can be well described using these reference spectra (Figure S10a). Anatase (23 – 46%), rutile (28 – 45%) and ilmenite (12 – 40%) were the dominant phases (Figure S10b). Ti(IV) sulfate contributed 15% to sample So2, collected from a Swiss coniferous forest. CaTiO_3 was not a relevant reference to reproduce the experimental data. The pre-edge and XANES features are better described compared to most sludge and all previously discussed ash samples (section 3.2.2 main text). XANES of Ti-phases containing ash is different from the corresponding soil spectra and has previously be discussed as a method to quantify the input of engineered TiO_2 -NP into agricultural soils (Pradas del Real et al., 2018). The authors did not include titanates (ATiO_3) into the analysis that proved relevant in the present study. Rather, an amorphous TiO_2 reference material spectrum which was similar to the Ti(IV)sulfate spectrum in shape was used.

TABLE S7. Information on the origin soil samples.

Reference name	NABO name	Soil usage
So1	74 MOE 1-5A I/1	Gras land, intensive
So2	76 SEN 1-5A II/1	Coniferous forest
So3	9 BR 1-7A I/1	Arable land
So4	27 JU 1-6A I/1	Deciduous forest.
So5	32 LB 1-6A I/1	Gras land, extensive
So6	79 LUG 1-5A II/1	Arable land

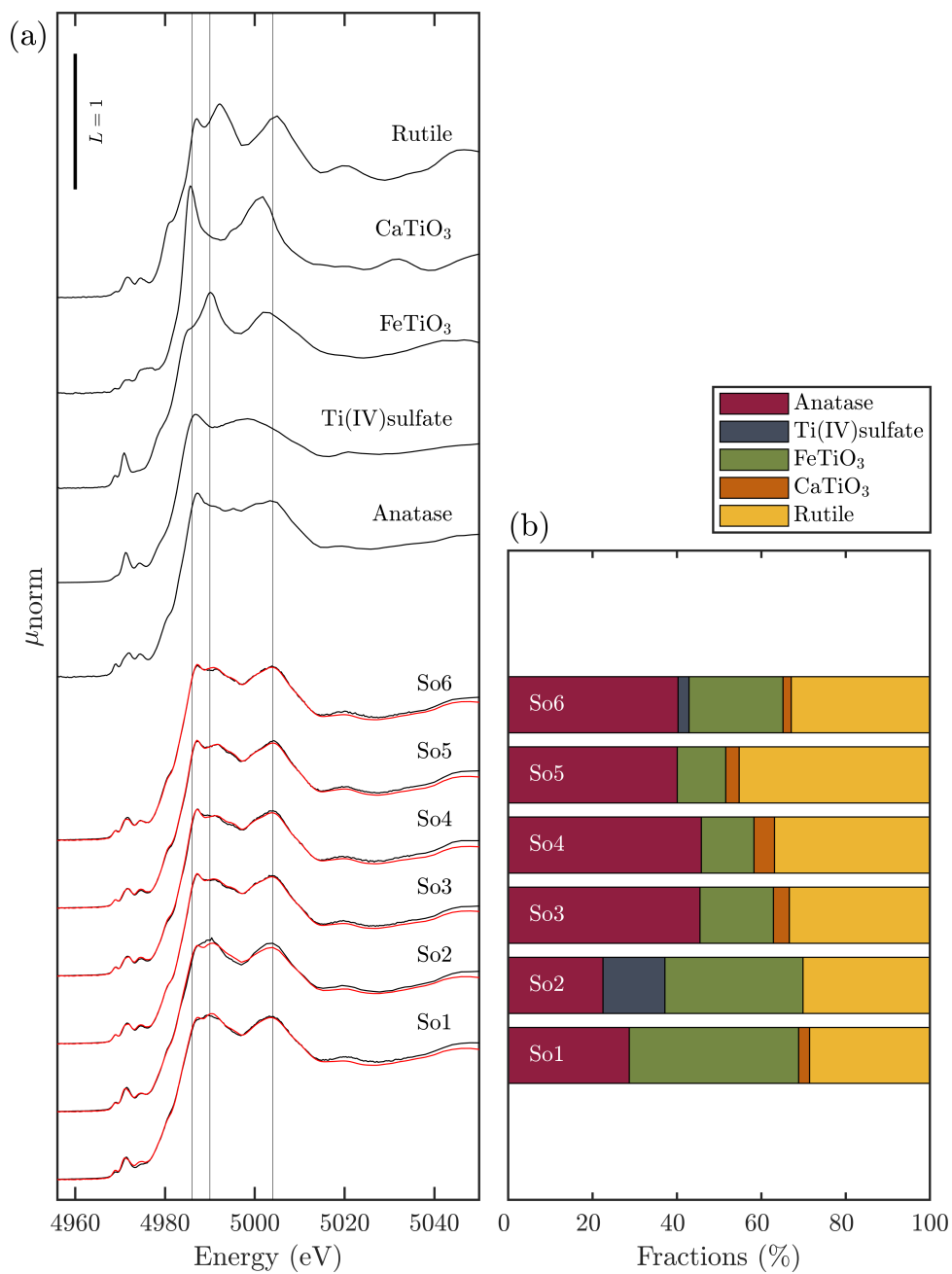


FIGURE S10. (a) XANES spectra of soil samples from the NABO soil repository (lower part, black), their corresponding LCF (red) and reference material spectra selected for LCF (upper part). The grey, vertical lines guide the eye. (b) displays the fractions corresponding to the spectra on the left.

S10 Supporting synchrotron XRF data on a related sample

The goal of this section was to provide data on the distribution of Ti over a larger area ($500 \times 500 \mu\text{m}$) with micron-scale resolution ($3 \times 3 \mu\text{m}$). A fly ash sample cut into epoxy embedded $30 \mu\text{m}$ thin sections, which were already prepared for a previously published study (Wielinski et al., 2020) (sample ASH NP, generated using the pilot fluidized bed reactor (Wielinski et al., 2019, 2020)) were used in this study. The data was recorded at the X05LA “microXAS” beamline at the Swiss Light Source at 18 keV. The spatial extensions of the beam were $3 \times 3 \mu\text{m}$. Details on the data collection can be found elsewhere (Wielinski et al., 2020). Here, only a Fe-Ti bicolor map (green/red) extracted from a larger dataset is presented (Figure S11). Although Ti seems to be entirely concentrated in a few hotspots (red), a significant share of the Ti counts originates from the Fe dominated area on the ash grains. Based on an analysis of the fraction of Ti present in the hotspots as a function of the definition of a hotspot (n Ti intensity/highest Ti intensity) two clearly distinct regimes become visible (Figure S12a). Setting a “pixel inclusion threshold” to 0.14 (vertical line, Figure S12a) of the maximum intensity leads to 5% of the total Ti cumulating in the hotspots. Comparing the pixels defined as being part of a hotspot (white pixels, Figure S12b) to the Ti rich regions (red, Figure S11) it can be seen that all relevant spots were included. This indicates that although micrometer sized Ti hotspots are present in the ash, diffusely distributed Ti accounts for $\approx 95\%$ of the total Ti in the map, in agreement with the sub-micron Ti domains observed in STEM/EDS data in sections 3.2.4 and 3.4 (both main text).

S11 Semi-quantitative Rietveld analysis of sample A-af

Semi-quantitative Rietveld analysis showed that in sample A-af hematite (27.4%) and a member of the whitlockite group (39.0%) constituted the most important mineral phases in agreement with high concentrations of Ca, Fe and P in the ash (Table S1, Figure S13, Figure S14). For the refinement of whitlockite, $\text{Ca}_9\text{Mg}(\text{PO}_4)_6(\text{HPO}_4)$ was used, although the phase present in the ash may have had a slightly different composition. The whitlockite structure is quite flexible, therefore, one may find Na, Fe and Sr substituting Ca and Mg in this structure. Further identified phases were AlPO_4 (14.0%), quartz (13.7%), anhydrite (3.1%) and gypsum (2.5%). The Ti-Fe containing phases had to low concentration to show up in the diffractograms. The sum of the phases was 99.7%, the weighted residual for the whole pattern (Rwp) was 3.5% and the goodness of fit (S) was 2.71, indicating that the fit was of good quality.

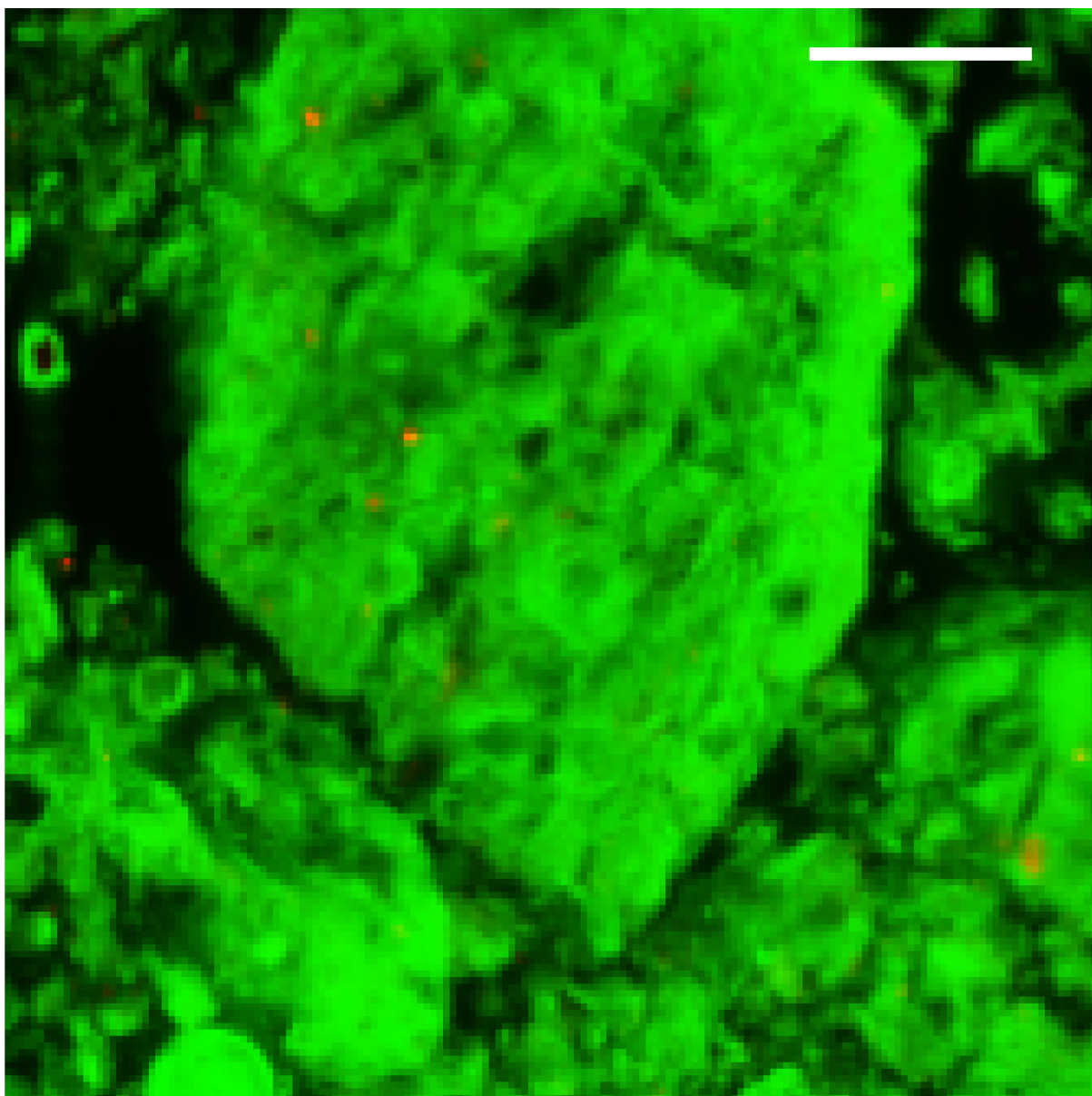


FIGURE S11. Bicolor map (green: Fe, red: Ti) of Ti and Fe distribution in fly ash generated using the pilot fluidized bed reactor. The white bar indicates a length of 100 μm .

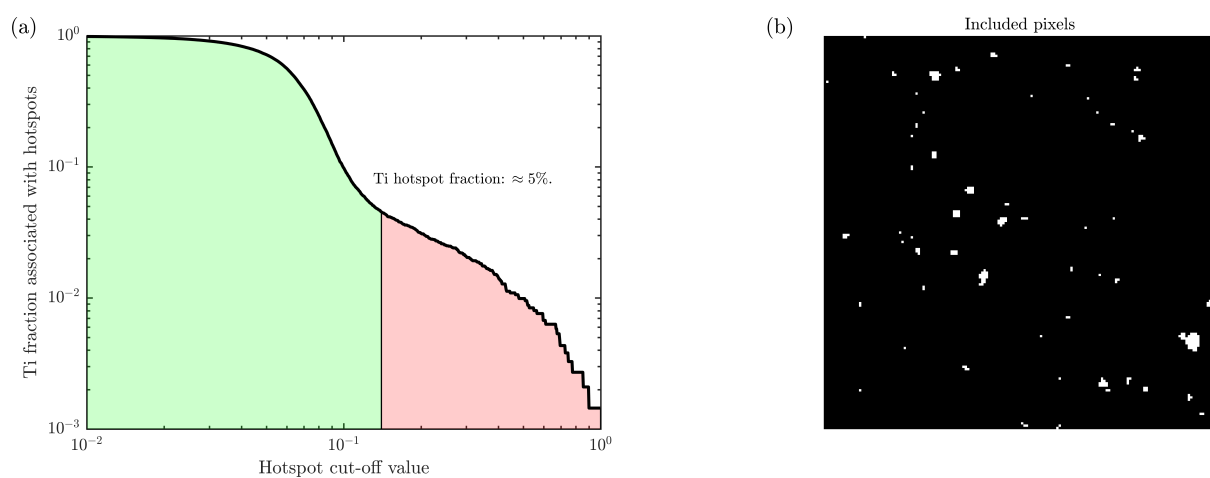


FIGURE S12. The fraction of Ti associated with the red hotspots in Figure S11 as a function of a variable cut-off value. (b) white spots indicate the pixels that were considered Ti hotspots.

References

- Köhler, J., R.Dinnebier, and A.Bussmann-Holder (2012). Structural instability of EuTiO_3 from X-ray powder diffraction. *Phase Transitions*, 85(11):949–955.
- Kravtsova, A., Soldatov, A., Nachtegaal, M., Tew, M., and van Bokhoven, J. (2010). Influence of the muffin-tin approximation on the simulation of titanium K-edge X-ray absorption spectra of TiO_2 (rutile and anatase phases). *Physica B: Condensed Matter*, 405(2):724 – 726.
- Pradas del Real, A. E., Castillo-Michel, H., Kaegi, R., Larue, C., de Nolf, W., Reyes-Herrera, J., Tucoulou, R., Findling, N., Salas-Colera, E., and Sarret, G. (2018). Searching for relevant criteria to distinguish natural vs. anthropogenic TiO_2 nanoparticles in soils. *Environmental Science: Nano*, 5:2853–2863.
- Scheinost, A. C. (2005). Metal oxides in *Encyclopedia of Soils in the Environment*. New York: Elsevier Academic Press, 428-438.
- Wielinski, J., Gogos, A., Voegelin, A., Müller, C., Morgenroth, E., and Kaegi, R. (2019). Transformation of nanoscale and ionic Cu and Zn during the incineration of digested sewage sludge (biosolids). *Environmental Science & Technology*, 53(20):11704–11713.
- Wielinski, J., Marafatto, F. F., Gogos, A., Scheidegger, A., Voegelin, A., Müller, C. R., Morgenroth, E., and Kaegi, R. (2020). Synchrotron hard X-ray chemical imaging of trace element speciation in heterogeneous samples: development of criteria for uncertainty analysis. *Journal of Analytical Atomic Spectrometry*, 35:567–579.